Magnetoinductive breathers in metamaterials

M. Eleftheriou,[1,2] N. Lazarides,[1,3] and G. P. Tsironis[1]

[1]*Department of Physics, University of Crete and Institute of Electronic Structure and Laser,*
Foundation for Research and Technology—Hellas, P.O. Box 2208, 71003 Heraklion, Greece

[2]*Department of Music Technology and Acoustics, Technological Educational Institute of Crete,*
E. Daskalaki, Perivolia, 74100 Rethymno, Crete, Greece

[3]*Department of Electrical Engineering, Technological Educational Institute of Crete,*
P.O. Box 140, Stavromenos, 71500 Heraklion, Crete, Greece

The existence and stability of discrete breathers (DBs) in one- and two-dimensional magnetic metamaterials (MMs), which consist of periodic arrangements (arrays) of split-ring resonators (SRRs), are investigated numerically. We consider different configurations of the SRR arrays, which are related to the relative orientation of the SRRs in the MM, in both one and two spatial dimensions. In the latter case we also consider anisotropic MMs. Using standard numerical methods we construct several types of linearly stable breather excitation in both Hamiltonian and dissipative MMs (dissipative breathers). The study of stability in both cases is performed using standard Floquet analysis. In both cases we find that the increase of dimensionality from one to two spatial dimensions does not destroy the DBs, which may also exist in the case of moderate anisotropy (in two dimensions). In dissipative MMs, the dynamics is governed by a power balance between the mainly Ohmic dissipation and driving by an alternating magnetic field. In that case it is demonstrated that DB excitation locally alters the magnetic response of MMs from paramagnetic to diamagnetic. Moreover, when the frequency of the applied field approaches the SRR resonance frequency, the magnetic response of the MM in the region of the DB excitation may even become negative (extremely diamagnetic).

PACS number(s): 41.20.Jb, 63.20.Pw, 75.30.Kz, 78.20.Ci

I. INTRODUCTION

Discrete breathers (DBs), also known as intrinsic localized modes, are genuine nonlinear excitations that oscillate for long times in a localized region of space and may be produced generically in discrete lattices of weakly coupled nonlinear elements (see [1] for a general review). Since their introduction [2], a large volume of analytical and numerical studies have explored the existence and the properties of DBs in a variety of discrete nonlinear systems. Rigorous mathematical proofs of existence of DBs in both Hamiltonian (i.e., energy conserved) and dissipative lattices of weakly coupled nonlinear oscillators have been given [3,4], and numerical algorithms for their accurate construction have been designed [5–7]. DBs may appear spontaneously in a lattice as result of fluctuations [8–10] or disorder [11], or by purely deterministic mechanisms [12]. They have been observed experimentally in several systems, including solid state mixed-valence transition metal complexes [13], quasi-one-dimensional antiferromagnetic chains [14], arrays of Josephson junctions [15], micromechanical oscillators [16], optical waveguide systems [17], and proteins [18]. Once generated, DBs modify system properties such as lattice thermodynamics, and introduce the possibility of nondispersive energy transport [19,20], because of their potential for translatory motion (i.e., mobility) along the lattice [21]. In numerical experiments DB mobility can be achieved by an appropriate perturbation [22]. Recently, experimental evidence has been found for moving DBs in a layered crystal insulator at 300 K [23] and in a small micromechanical cantilever array [24]. From the perspective of applications to experimental situations where dissipative effects are always

present, dissipative DB excitations (usually driven by an alternating power source) are more relevant than their Hamiltonian counterparts. Dissipative DBs, which possess the character of an attractor for initial conditions in the corresponding basin of attraction, may appear whenever power balance, instead of energy conservation, governs the nonlinear dynamics of the lattice. Furthermore, the attractor character of dissipative DBs allows for the existence of quasiperiodic and even chaotic DBs [25,26].

Recently, dissipative DBs have been demonstrated numerically in discrete and nonlinear magnetic metamaterials (MMs) driven by an alternating electromagnetic (EM) field [27]. The MMs are artificially structured materials that exhibit EM properties not available in naturally occurring materials. The response of any material (either natural or artificial) to applied EM fields is characterized by macroscopic parameters such as the electric permittivity ϵ and the magnetic permeability μ. For example, there are only a few natural materials responding magnetically at terahertz (THz) and optical frequencies, and that response is usually very weak. However, the MMs exhibit relatively large magnetic response at those frequencies [28–30], which may be either positive or negative, resulting in positive or negative μ, respectively. The realization of MMs at such frequencies will certainly affect THz optics and its applications, while it promises new device applications. The most common element utilized for magnetic response from MMs is the split-ring resonator (SRR) which, in its simplest form, is a metallic ring with one slit, made of a highly conducting metal. Periodic SRR arrays at the nanoscale, a genuine realization of MMs, are fabricated routinely using conventional microfabrication techniques. These MMs, in which the SRRs are weakly coupled magnetically through their mutual induc-

tances, support a new type of guided waves, the magnetoinductive (MI) waves [31–34]. The MI waves propagate within a band near the resonant frequency of the SRRs, and exist as forward and backward waves depending on the orientation of the elements (e.g., the SRRs) of the MM [31]. In the linear regime of MI wave propagation in a MM, the magnetic permeability μ does not depend on the intensity of the EM field. However, the MMs may become nonlinear, either by embedding the SRRs in a Kerr-type medium [35,36], or by inserting certain nonlinear elements (e.g., diodes) in each SRR [37–39]. Then, the combined effects of nonlinearity and discreteness (inherent in SRR-based MMs), leads in the generation of nonlinear excitations in the form of DBs [27], as well as magnetic domain walls [40], and magnetoinductive envelope solitons [41]. The latter may be either bright or dark, and they result from the modulational instability of the MI waves. While the nonlinearity by itself offers tunability, stationary (i.e., not mobile, pinned) DBs act as stable impurity modes that are dynamically generated and may alter propagation and emission properties of a system. Moreover, stationary dissipative DBs can change locally the magnetic response of a nonlinear MM [27]. We should also note that regular arrays of rf superconducting quantum interference devices (SQUIDs) offer an alternative for the construction of nonlinear MMs due to the nonlinearity of the Josephson junction [42].

In the present work we investigate numerically the existence and stability of both dissipative and energy-conserved DBs in discrete, periodic arrays of nonlinear SRRs. We consider different SRR array geometries (i.e., different orientations of the SRRs in the MM) in one and two spatial dimensions. In two dimensions we also consider several cases of possible anisotropy. In the next section we describe the discrete MM model, while in Sec. III we construct several types of DBs for one-dimensional (1D) arrays. Here we also calculate the magnetic response, which may be locally altered by the presence of a DB. In Sec. IV we construct several types of DBs for two-dimensional (2D) arrays, and we finish in Sec. V with the conclusions.

II. MAGNETIC METAMATERIAL MODEL

We consider 1D and 2D discrete, periodic arrays of identical nonlinear SRRs, which constitute the simplest realization of a MM in one and two dimensions [43], respectively. In one dimension, the SRRs form a linear array with their centers separated by distance d. In two dimensions, the SRRs are assumed to be arranged in a regular rectangular lattice, with their centers separated by distances d_x and d_y in the x and y directions, respectively (i.e., lattice constants d_x and d_y, respectively). There are two configurations of interest in each case, shown schematically in Figs. 1 and 2 for the 1D and 2D arrays, respectively. A 1D array can be constructed either in the planar configuration, where all SRR loops are in the same plane with their centers lying on a straight line [Fig. 1(a)], or in the axial configuration, where the line connecting the centers of the SRR loops is perpendicular to the plane of the loops [Fig. 1(b)] [31,33,34]. Similarly, a 2D array can be constructed either in the planar configuration, where all SRR
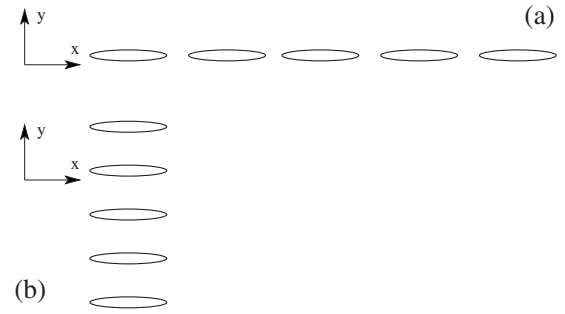

FIG. 1. Schematic view of a one-dimensional array of split-ring resonators in (a) the planar and (b) the axial geometry [31,33,34]. In both geometries the split-ring resonator axes as well as the magnetic component of the applied field are directed along the y axis. The electric field component is transverse to the slits (not shown in the figure).

loops are in the same plane with their centers located on an orthogonal lattice [Fig. 2(a)], or in the planar-axial configuration, where all SRRs have the planar configuration in one direction while they have the axial configuration in the other direction [Fig. 2(b)] [31,33,34].

Within good approximation, each SRR is equivalent to a nonlinear resistor-inductor-capacitor (*RLC*) circuit featuring a self-inductance L, Ohmic resistance R, and capacitance C. The units (i.e., the SRRs) become nonlinear due to a Kerr dielectric filling the SRRs' slits, whose permittivity ϵ is of the form

$$\epsilon(|\mathbf{E}|^2) = \epsilon_0 \left(\epsilon_\ell + \alpha \frac{|\mathbf{E}|^2}{E_c^2} \right), \tag{1}$$

where $\mathbf{E}$ is the electric field, E_c is a characteristic (large) electric field, ϵ_ℓ is the linear permittivity, ϵ_0 is the permittivity of the vacuum, and $\alpha = +1$ (-1) corresponds to self-focusing (self-defocusing) nonlinearity. As a result, the SRRs acquire a field-dependent capacitance $C(|\mathbf{E}|^2) = \epsilon(|\mathbf{E}_g|^2) A / d_g$, where A is the area of the cross section of the SRR wire, $\mathbf{E}_g$ is the electric field induced along the SRR slit, and d_g is the size of the slit. The origin of $\mathbf{E}_g$ may be due to the magnetic and/or the electric components of the applied EM field, depending on the relative orientation of that field with respect to the SRRs' plane and the slits. In the following we assume
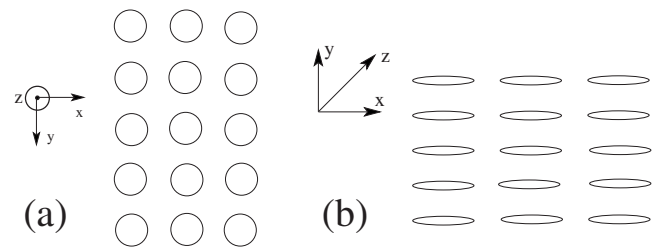

FIG. 2. Schematic view of a two-dimensional array of split-ring resonators in (a) the planar and (b) the planar-axial geometry [31,33,34]. In both geometries the magnetic component of the applied field is directed along the SRR axes, while the electric field component is transverse to their slits (not shown in the figure).

that, for any array configuration and number of dimensions, the magnetic component of the incident (applied) EM field is always perpendicular to the SRRs' plane, and that the electric component of the incident EM field is transverse to the slit. Then, only the magnetic component excites an electromotive force (emf) in the SRRs, resulting in an oscillating current in each SRR loop and the corresponding development of an oscillating voltage difference U across the slits or, equivalently, of an oscillating electric field $\mathbf{E}_g$ in the slits. If Q is the charge stored in the capacitor of an SRR then, from the general relation of a voltage-dependent capacitance, $C(U) = dQ/dU$, and Eq. (1), we get

$$Q = C_\ell \left(1 + \alpha \frac{U^2}{3\epsilon_\ell U_c^2} \right) U, \tag{2}$$

where $U = d_g E_g$, $C_\ell = \epsilon_0 \epsilon_\ell (A/d_g)$ is the linear capacitance, and $U_c = d_g E_c$. Assume that the arrays are placed in a time-varying and spatially uniform magnetic field of the form

$$H = H_0 \cos(\omega t), \tag{3}$$

where H_0 is the field amplitude, ω is the field frequency, and t is the time variable. The excited emf $\mathcal{E}$, which is the same in all SRRs, is given by

$$\mathcal{E} = \mathcal{E}_0 \sin(\omega t), \quad \mathcal{E}_0 \equiv \mu_0 \omega S H_0, \tag{4}$$

where S is the area of each SRR loop and μ_0 the permeability of the vacuum. Each SRR in the field given by Eq. (3) is a nonlinear oscillator that exhibits a resonant magnetic response (either positive or negative) at a particular frequency which is very close to its linear resonance frequency $\omega_\ell = 1/\sqrt{LC_\ell}$ (for $R \simeq 0$).

All SRRs in an array are coupled together due to magnetic interaction through their mutual inductances [44]. However, we assume below only nearest neighbor interactions, so that neighboring SRRs are coupled through their mutual inductances M_x and M_y. This is a very good hypothesis in the planar configurations (i.e., in both 1D and 2D arrays), even if the SRRs are very close. The validity of the nearest neighbor approximation for the other configurations (i.e., the axial configuration in 1D arrays and the planar-axial configuration in 2D arrays) has been checked by taking into account the interaction of the SRRs with their four nearest neighbors, using the fact that the mutual inductance $M_{x,y}^{(s)}$ between a SRR and its sth neighbor varies as $M_{x,y}^{(s)} \simeq M_{x,y}/s^3$. We found that for weak coupling, as we consider here, the results are practically the same as those obtained with the nearest neighbor approximation. The issue of validity of the nearest neighbor approximation in periodic chains of magnetically coupled L-C resonators has been discussed in detail in Ref. [45]. There, it was concluded that, for matching theory to experiment, it is necessary to take into account higher-order interactions, i.e., the interactions of each resonator with a number of its neighbors. Thus, the electrical equivalent of a SRR array in an alternating magnetic field is an array of nonlinear RLC oscillators coupled with their nearest neighbors through mutual inductances, which are driven by identical alternating voltage sources. Therefore the equations describing the dynamics of the charge $Q_{n,m}$ and the current $I_{n,m}$

circulating in the (n,m)th SRR may be derived simply from Kirchhoff's voltage law for each SRR [27,40],

$$\frac{dQ_{n,m}}{dt} = I_{n,m}, \tag{5}$$

$$L\frac{dI_{n,m}}{dt} + RI_{n,m} + f(Q_{n,m})$$
$$= -M_x\left(\frac{dI_{n-1,m}}{dt} + \frac{dI_{n+1,m}}{dt} \right) - M_y\left(\frac{dI_{n,m-1}}{dt} + \frac{dI_{n,m+1}}{dt} \right) + \mathcal{E}, \tag{6}$$

where $f(Q_{n,m}) = U_{n,m}$ is given implicitly by Eq. (2). Using the relations

$$\omega_\ell^{-2} = LC_\ell, \quad \tau = t\omega_\ell, \quad I_c = U_c \omega_\ell C_\ell, \quad Q_c = C_\ell U_c, \tag{7}$$

$$\mathcal{E} = U_c \varepsilon, \quad I_{n,m} = I_c i_{n,m}, \quad Q_{n,m} = Q_c q_{n,m}, \tag{8}$$

and Eq. (4), Eqs. (5) and (6) can be normalized to

$$\frac{dq_{n,m}}{d\tau} = i_{n,m}, \tag{9}$$

$$\frac{di_{n,m}}{d\tau} + \gamma i_{n,m} + f(q_{n,m}) + \lambda_x\left(\frac{di_{n-1,m}}{d\tau} + \frac{di_{n+1,m}}{d\tau} \right)$$
$$+ \lambda_y\left(\frac{di_{n,m-1}}{d\tau} + \frac{di_{n,m+1}}{d\tau} \right) = \varepsilon_0 \sin(\Omega\tau), \tag{10}$$

where $\gamma = RC_\ell \omega_\ell$ is the loss coefficient, $\lambda_{x,y} = M_{x,y}/L$ are the coupling parameters in the x and y directions, respectively, and $\varepsilon_0 = \mathcal{E}_0/U_c$. Note that the loss coefficient γ, which is usually very small ($\gamma \ll 1$), may account for both Ohmic and radiative losses [41]. The corresponding equations for 1D arrays result from Eqs. (9) and (10), i.e., by setting $\lambda_y = 0$, dropping the subscript m, and choosing the appropriate $\lambda_x = \lambda$. Neglecting losses and without applied field, Eqs. (9) and (10) can be derived from the Hamiltonian

$$\mathcal{H} = \sum_{n,m}\left(\frac{1}{2}\dot{q}_{n,m}^2 + V_{n,m} \right) - \sum_{n,m}(\lambda_x \dot{q}_{n,m}\dot{q}_{n+1,m} + \lambda_y \dot{q}_{n,m}\dot{q}_{n,m+1}), \tag{11}$$

where the nonlinear on-site potential $V_{n,m}$ is given by

$$V_{n,m} \equiv V(q_{n,m}) = \int_0^{q_{n,m}} f(q'_{n,m})dq'_{n,m}, \tag{12}$$

and $\dot{q}_{n,m} \equiv dq_{n,m}/d\tau$. Analytical solution of Eq. (2) for $u_{n,m} = f(q_{n,m})$ with the conditions of $u_{n,m}$ being real and $u_{n,m}(q_{n,m} = 0) = 0$ gives the approximate expression

$$f(q_{n,m}) \simeq q_{n,m} - \frac{\alpha}{3\epsilon_\ell}q_{n,m}^3 + 3\left(\frac{\alpha}{3\epsilon_\ell} \right)^2 q_{n,m}^5, \tag{13}$$

which is valid for relatively low q_n ($q_n < 1$, $n = 1, 2, \ldots, N$) Thus, the on-site potential is soft for $\alpha = +1$ and hard for $\alpha = -1$. In the 2D case the mutual inductances M_x and M_y may differ in both their sign, depending on the configuration, and

their magnitude. Actually, even in the planar 2D configuration with $d_x = d_y$ considerable anisotropy may result in the coupling parameters in the x and y directions. The reason is that the coupling of the SRRs results from both magnetic and electric mechanisms, which, for the planar geometry, may become positive or even complex, depending on the relative distance between the SRRs and their orientation [46]. This anisotropy can be effectively taken into account by considering different coupling parameters λ_x and λ_y. The coupling parameters $\lambda_{x,y}$ as well as the loss coefficient γ can be calculated numerically for this specific model with high accuracy. However, for our purposes, it is sufficient to estimate these parameters for realistic (experimental) array parameters. The self-inductance of a circular SRR of radius a (with circular cross section of diameter h) can be determined by the well-known expression $L = \mu_0 a[\ln(16a/h) - 1.75]$. The value of the capacitance then follows from the choice of the resonance frequency ω_ℓ. (We ignore the effects of nonlinearity and coupling between the SRRs on the resonance frequency.) The resistance can be calculated from the given SRR dimensions and the appropriate value of the conductivity, taking into account the skin effect. The expression for the mutual inductance between two loops can be calculated by means of a simple approximation [27]. For example, for an array of circular silver-made SRRs with circular cross section in the planar geometry, with geometrical and material parameters close to those in Ref. [43] (for the equivalent squared SRR with squared cross section), it has been estimated that $\lambda \approx 0.02$ and $\gamma \approx 0.01$ [27]. For the same SRRs in the axial geometry, separated by distance d like those in the planar geometry, the approximate expressions for the mutual inductance and the coupling parameter are $M \simeq (\pi/2)\mu_0 a(a/d)^3$ and $\lambda \simeq (\pi/2)\mu_0 a(a/d)^3/L$, respectively. Those expressions are obtained by making the same approximations as in Ref. [27], and knowing that the magnetic field of one of the SRRs with induced current I at the center of the other SRR, which is directed along its axis, is given by $B = \mu_0 I a^2/2(a^2 + d^2)^{3/2}$. Thus, the coupling of two SRRs in the axial geometry is stronger (by a factor of 2) than that of the same SRRs in the planar geometry. Of course that result represents only a rough approximation of the relative strengths of the couplings in the planar and axial geometries. Although it correctly predicts that the coupling is stronger in the latter case [31], it does not give accurate quantitative information. For that, we refer to [44], where the coupling strengths for both geometries have been calculated for a rather wide d/a interval [see their Fig. 1(a)].

For the integration of Eqs. (9) and (10), in both the Hamiltonian and the damped driven cases, or the corresponding linearized ones, we use a standard fourth-order Runge-Kutta algorithm with fixed time stepping Δt (typically $\Delta t = 0.01$). Since the DBs studied here are highly localized, the choice of boundary conditions to be imposed on Eqs. (9) and (10) is not especially important. Thus, we have chosen periodic boundary conditions throughout the study.

III. DISCRETE BREATHERS IN ONE-DIMENSIONAL SRR ARRAYS

We consider the two different 1D configurations of SRR arrays shown in Fig. 1, with the same number of SRR oscillators $N = 50$. Within the equivalent circuit model, the difference between the two configurations resides in the sign and the magnitude of the coupling parameter λ. In the planar geometry (configuration) λ is negative, since the mutual inductance M between two neighboring SRRs is negative. This is because the magnetic field generated by one SRR (due to the current induced in its loop) crosses the neighboring SRR in the opposite direction. For the axial geometry, the mutual inductance M, and hence λ, is positive. Moreover, in a 1D array of SRRs in the axial geometry, the value of λ is much higher than that in a 1D array of SRRs in the planar geometry with the same SRR spacing d [31,44]. High coupling between SRRs in the axial geometry would possibly require taking into account the interaction of an SRR with its far neighbors (and not only with its nearest neighbors) [45]. To avoid such complications, and for the sake of comparison of the DBs obtained in the two geometries, we assume that the SRR spacing is such that the magnitude of the coupling between neighboring SRRs is the same (or at least of the same order) in both geometries.

For Hamiltonian systems, DBs may be constructed from the anticontinuous limit [5], where all the SRRs are uncoupled ($\lambda \to 0$), obeying identical dynamical equations. Fixing the amplitude of one of them (say the one located at $n = n_b$) to a specific value q_b, with the corresponding current $i_b = 0$, we can determine, either analytically (if possible) or numerically, the period of oscillation T_b. An initial condition with $q_n = 0$ for any $n \neq n_b$, $q_{n_b} = q_b$, and $\dot{q}_n = i_n = 0$ for any n, represents a trivial DB with period T_b. Continuation of this solution for $\lambda \neq 0$ using the Newton method [5] results in numerically exact DBs up to a maximum value of the coupling parameter $\lambda = \lambda_{max}$. For the existence of Hamiltonian DBs it is required that the DB frequency $\omega_b = 2\pi/T_b$, as well as all its multiples, lie outside the linear dispersion band of MI waves. The MI wave band is obtained by substituting a plane wave of the form $q_n = A \cos(\kappa n - \Omega \tau)$ into the linearized equations (9) and (10) (with $\varepsilon = 0$, $\gamma = 0$),

$$\Omega_\kappa = \frac{1}{\sqrt{1 + 2\lambda \cos(\kappa)}}, \qquad (14)$$

where $\Omega = \omega/\omega_\ell$ is the normalized frequency, and $\kappa = kd$ is the normalized wave number ($-\pi \leq \kappa \leq \pi$). Typical dispersion curves are shown in Fig. 3 for both geometries. For $|\lambda| \ll 1$ the band is very narrow (bandwidth $\Delta\Omega \simeq 2|\lambda|$), so that the requirement for the existence of Hamiltonian DBs can be easily satisfied. Clearly, the bandwidth increases with increasing λ. The MI waves are forward in the axial configuration ($\lambda > 0$) with codirectional phase and group velocities, and backward in the planar configuration ($\lambda < 0$), with phase and group velocities in the opposite directions [31].

Following the procedure described above, with the appropriate choice of initial conditions (trivial DBs), we have constructed several types of Hamiltonian, numerically exact DBs for 1D SRR arrays in both the planar and the axial geometries, shown in Figs. 4(a)–4(d) and 5(a)–5(d) for self-focusing ($\alpha = +1$) and self-defocusing nonlinearities ($\alpha = -1$), respectively. Those Hamiltonian DB profiles (shown at maximum amplitude), i.e., the normalized current i_n as a
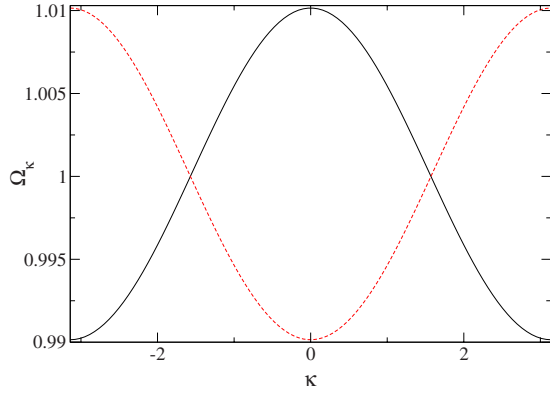
FIG. 3. (Color online) Frequency spectrum of linear MI waves Ω_κ as a function of the wave number κ, for $\lambda=-0.01$ (black solid curve) and $+0.01$ (red dashed curve).

function of array site n, are characterized as single-site bright DBs [Figs. 4(a) and 5(a)], antisymmetric bright DBs [Figs. 4(b) and 5(b)], single-site dark DBs [Figs. 4(c) and 5(c)], and bright multibreathers [Figs. 4(d) and 5(d)]. The term "bright" ("dark") DBs is used when there are only one or a few SRRs in which the current oscillates with large (small) amplitude, whereas the rest of them oscillate with small (large) amplitude [48]. All these DBs are highly localized, occupying only a few lattice sites, since they have been obtained for low values of the coupling parameter λ. They are all symmetric, except those in Figs. 4(b) and 5(b), which are antisymmetric. It is interesting to observe that, for self-focusing nonlinearity ($\alpha=+1$), the profile of the single-site bright DB [Fig. 4(a)] is staggered (unstaggered) for SRR arrays in the planar (axial) geometry, while, for self-defocusing nonlinearity ($\alpha=-1$),
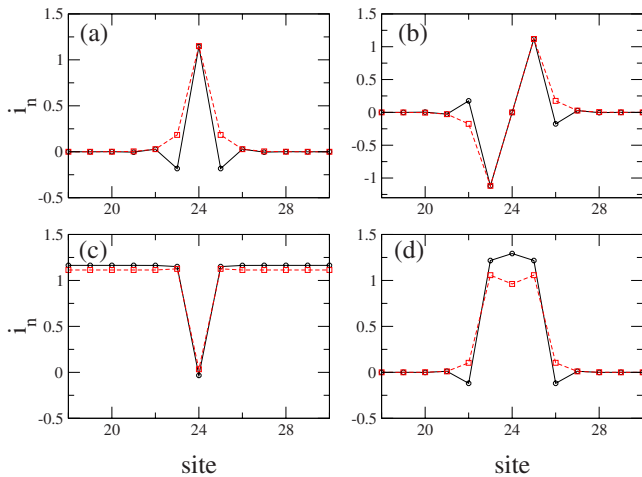

FIG. 4. (Color online) Several Hamiltonian discrete breather profiles (at maximum amplitude) for $\alpha=+1$, $\Omega_b=0.938$, $\epsilon_\ell=2$, $N=50$, constructed with Newton's method for both the planar and the axial array configurations [shown as black circles and red (gray) squares, respectively]. (a) A single-site bright breather for $|\lambda|=0.02$; (b) an antisymmetric bright breather for $|\lambda|=0.02$; (c) a single-site dark breather for $|\lambda|=0.002$; and (d) a bright multibreather for $|\lambda|=0.013$. Only part of the simulated array is shown for clarity.
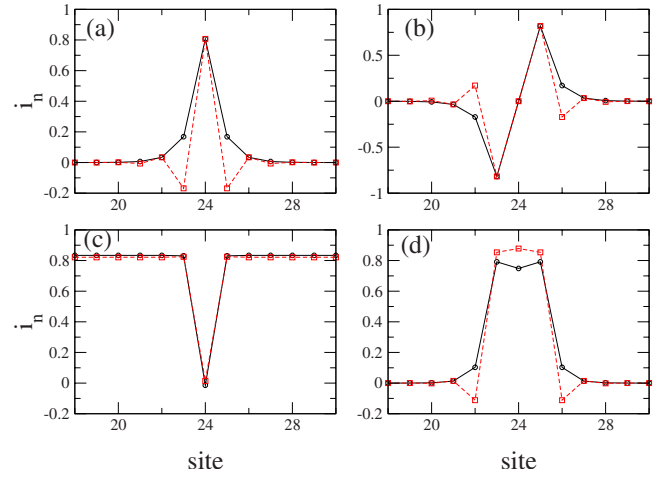

FIG. 5. (Color online) Several Hamiltonian discrete breather profiles (at maximum amplitude) for $\alpha=-1$, $\Omega_b=1.056$, $\epsilon_\ell=2$, $N=50$, constructed with Newton's method for both the planar and the axial array configurations [shown as black circles and red (gray) squares, respectively]. (a) A single-site bright breather for $|\lambda|=0.02$; (b) an antisymmetric bright breather for $|\lambda|=0.02$; (c) a single-site dark breather for $|\lambda|=0.001$; and (d) a bright multibreather for $|\lambda|=0.013$. Only part of the simulated array is shown for clarity.

the profile of the single-site bright DB Fig. 5(a)] is staggered (unstaggered) for SRR arrays in the axial (planar) geometry. Recall that a staggered (unstaggered) DB is one whose profile is of the form $i_n=\mathcal{I}_n\exp[i\kappa_b(n-n_b)]$, $\mathcal{I}_n=|i_n|>0$, with $\kappa_b=\pi$ ($\kappa_b=0$) [49]. The single-site DBs in Figs. 4(a) and 5(a), with (normalized) frequencies $\Omega_b=\omega_b/\omega_\ell=0.938$ and 1.056, respectively, may be continued for higher values of coupling. They cease to exist when the MI wave band, which expands with increasing λ, reaches the DB frequency Ω_b. That will occur at $|\lambda|=|\lambda_{max}|=|1-1/\Omega_b^2|/2$, which gives $|\lambda_{max}|\simeq0.068$ and 0.052 for $\Omega_b=0.938$ and 1.056, respectively.

The linear stability of Hamiltonian DBs is addressed through the eigenvalues of the Floquet matrix (Floquet multipliers). A DB is linearly stable when all its Floquet multipliers lie on a circle of radius unity in the complex plane. The DBs shown in Figs. 4(a), 4(b), 5(a), and 5(b) are all linearly stable. However, the dark DBs shown in Figs. 4(c) and 5(c) as red (gray) squares, as well as the multibreathers shown in Figs. 4(d) and 5(d) as red (gray) squares and black circles, respectively, are linearly unstable. Those DBs were found to be linearly stable only for very low couplings.

Next, we construct DBs for SRR arrays which are subjected to losses (damping) and the external driving force $\varepsilon(\tau)$ (dissipative DBs). In order to generate DBs in this case we start by solving Eqs. (9) and (10) in the anticontinuous limit, where all SRRs are uncoupled. We identify two coexisting (and stable) attractors of a single damped driven SRR oscillator with focusing nonlinearity ($\alpha=+1$) and $\Omega=0.92$, $\varepsilon_0=0.04$, $\gamma=0.01$, which have different amplitudes $q_h\simeq1.6086$ and $q_\ell\simeq0.2866$ (high- and low-amplitude attractors, respectively). Notice that the frequency Ω is below the SRR resonance frequency, where a MM is expected to show

only positive magnetic response (i.e., response corresponding to positive μ). Subsequently, we fix the amplitude of one of the SRR oscillators (say the one at $n=n_b$) to q_h and all the others to q_ℓ (i_n are all set to zero). Using this configuration (trivial dissipative DB) as initial condition, we start integrating Eqs. (9) and (10), while increasing the coupling parameter λ in small steps. In this way, the initial condition can be continued for $\lambda \neq 0$ leading to dissipative DB formation [5]. The time evolution of typical dissipative (single-site) bright DBs is shown for SRR arrays in the planar and the axial geometries in Fig. 6 (top and middle panels, respectively). We see that the DB and the background are oscillating with different amplitudes (high and low, respectively). In this aspect, dissipative DBs differ from their Hamiltonian single-site counterparts, where the background is always zero. We should note here that the DB frequency in this case is the same as that of the driving field, i.e., $\Omega_b \equiv 2\pi/T_b = \Omega$. However, the phase differences of the SRR oscillators in an array with respect to the driving field are generally different, so that a DB may change the magnetic response of an array locally, as we shall see below. We also note that the time evolution of the central DB site and the background is practically sinusoidal (harmonic), as can be seen, e.g., in Fig. 7 (red solid curves). This may not be true for other magneto-inductive systems such as magnetically coupled arrays of rf SQUIDs [47]. The bottom panels of Fig. 6 show two snapshots taken at maximum breather amplitude for the DBs presented in the top panel [Fig. 6(a)] and the middle panel [Fig. 6(b)] which can be compared with the corresponding Hamiltonian DBs shown in Fig. 4(a). Although the frequency Ω_b of those Hamiltonian DBs ($\sim$0.94) is not exactly equal to that of the dissipative DBs ($\sim$0.92), we can still make a quantitative comparison. The amplitudes of the dissipative DBs are higher than those of their Hamiltonian counterparts. The main difference, however, is seen in the DB tails. At maximum amplitude of the central DB site, the tails attain approximately their minimum (negative) value, due to the phase difference between the central DB site and the background. With appropriate initial conditions we can also obtain multibreathers where two or more sites oscillate with high (low) amplitude, and the others with low (high) amplitude.

The linear stability of the dissipative DBs can be addressed (as in the Hamiltonian case) through the eigenvalues of the Floquet matrix (Floquet multipliers). In the dissipative case, however, a DB is linearly stable when all its Floquet multipliers lie on a circle of radius $R_f = \exp(-\gamma T_b/2)$ in the complex plane [6], due to the presence of a dissipative term in the linearized equations of motion. Both the dissipative DBs shown in Fig. 6 are linearly stable. In order to check that result, we have also added small perturbations to these DBs (of the order of 10^{-2} of the DB amplitude) and let them evolve in time. We have followed the perturbed DBs over $10^3 T_b$ time units, observing that the DBs restore their unperturbed shape. In general, dissipative DBs have been found to exist for couplings λ much less than those of their Hamiltonian counterparts, λ_{max}. The DBs shown in Fig. 6 for dissipative and forced SRR arrays in the planar and the axial geometries are found to exist up to $\lambda \simeq 0.024$ and 0.017,
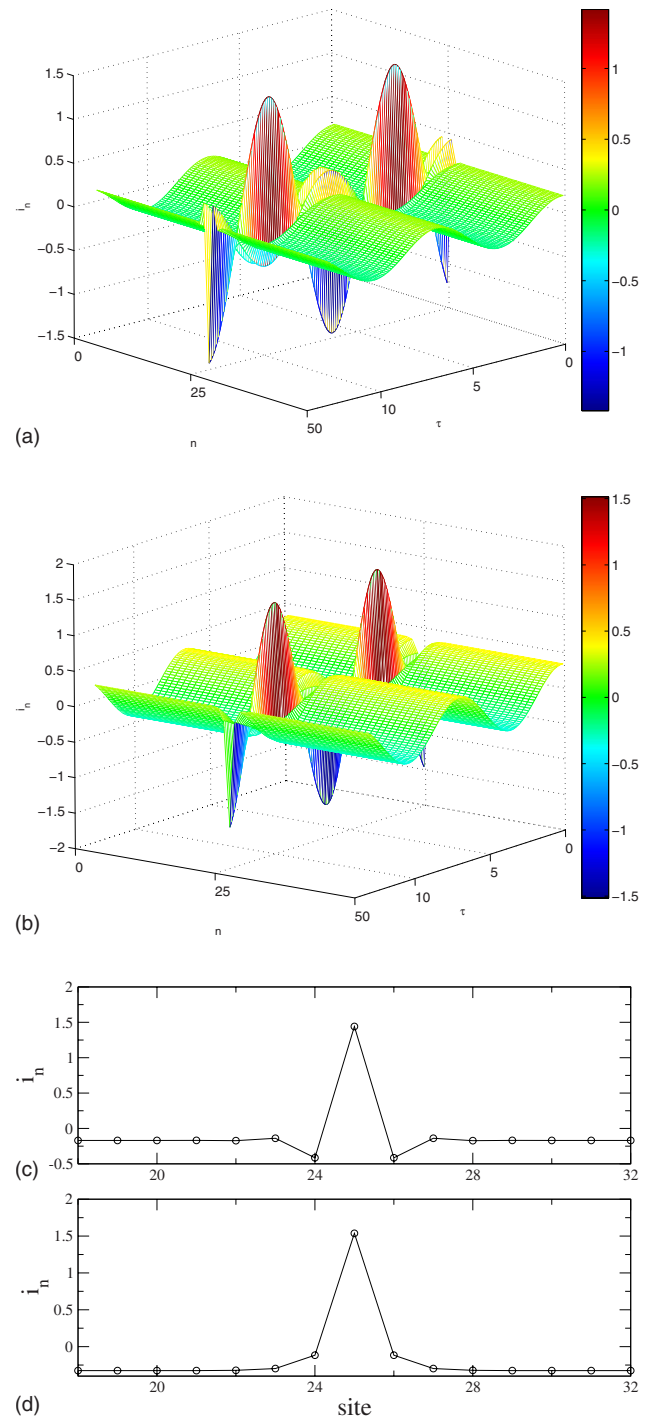

FIG. 6. (Color online) Time evolution of a single-site bright dissipative breather during approximately two periods, for $\alpha = +1$, $\Omega_b = 0.92$, $\varepsilon_0 = 0.04$, $\gamma = 0.01$, $\epsilon_\ell = 2$, $N = 50$, and (top panel) planar SRR array geometry with $\lambda = -0.02$; (middle panel) axial SRR array geometry with $\lambda = 0.017$. Bottom panels: snapshots (taken at maximum amplitude) of i_n as a function of the lattice site n for the dissipative breathers shown in (c) the top panel and (d) the bottom panel. Only part of the simulated array is shown for clarity.

respectively. For defocusing nonlinearity ($\alpha = -1$), it was impossible to identify two different-amplitude attractors and, thus, we were not able to construct dissipative DBs in this case.
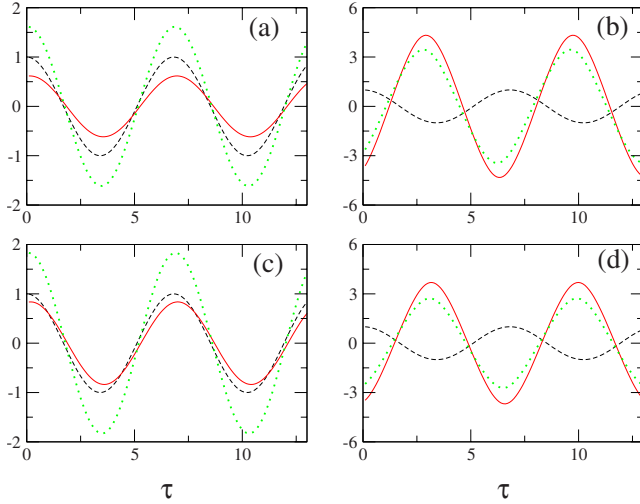
FIG. 7. (Color online) Time evolution of $\ell i_n(\tau)$ (red solid curve), compared with $\cos(\Omega\tau)$ (black dashed curve), and their sum (green dotted curve), during two breather periods, for (a) a 1D SRR array in the planar configuration at $n=15$ ($\lambda=-0.02$, $\ell=3$); (b) a 1D SRR array in the planar configuration at $n=n_b$ ($\lambda=-0.02$, $\ell=3$); (c) a 1D SRR array in the axial configuration at $n=15$ ($\lambda=0.017$, $\ell=2.4$); (d) a 1D SRR array in the axial configuration at $n=n_b$ ($\lambda=0.017$, $\ell=2.4$). The other parameters are as in Fig. 6.

It is interesting to calculate the magnetization in a dissipative SRR array. In the direction perpendicular to the SRR planes the general relation

$$B = \mu_0(H + \mathcal{M}) \qquad (15)$$

holds, with $\mathcal{M}=SI/d^3$ the magnetization (magnetic moment per unit cell volume) of the array. Equation (15), with use of Eq. (3), can be written in normalized form as

$$B/B_0 = \cos(\Omega\tau) + \ell i(\tau), \qquad (16)$$

where $B_0=\epsilon_0 U_c/S\omega$ and $\ell=\mu_0 S^2\Omega/\epsilon_0 d^3 L$. Equation (16) may be used locally at each cell, with the three terms B/B_0, $\cos(\Omega\tau)$, and $\ell i(\tau)$ representing the instantaneous magnetic induction, applied magnetic field, and magnetic response (local magnetization), respectively, in a specific cell. Negative magnetic response appears, as is apparent from Eq. (16), whenever the second term on the right-hand-side of Eq. (16) is larger in magnitude than the first one, and has the opposite sign. In Fig. 7 the time evolution is shown separately for each of the three terms of Eq. (16), i.e., the quantities $\ell i_n(\tau)$ (red solid curve), $\cos(\Omega\tau)$ (black dashed curve), and their sum B/B_0 (green dotted curve), for two different sites in both the planar and the axial geometries. Specifically, Figs. 7(a) and 7(b) are for the planar geometry, for $n=15$ (a site on the background, quite far away from the central DB site) and $n=n_b$ (DB central site), respectively, while Figs. 7(c) and 7(d) are for the axial geometry, for $n=15$ and $n=n_b$, respectively. We observe that, in both geometries, the SRR with low-amplitude current oscillation (reduced nonlinearity) shows positive (paramagnetic) response [Figs. 7(a) and 7(c) for the planar and the axial geometry, respectively], while the SRR with high-amplitude current oscillation (enhanced nonlinear-

ity) shows extreme diamagnetic (negative) response [Figs. 7(b) and 7(d) for the planar and the axial geometry, respectively]. Thus, in the breather or multibreather location, the lattice has a negative magnetic response even though it is driven below resonance. That result can be extended to uniform solutions, where $I_n=I$ for all n. Without nonlinearity such a solution always provides positive response below the resonance frequency ($\sim\omega_\ell$). However, the nonlinearity makes it possible to have two different coexisting and stable states (bistability) with low- and high-amplitude current oscillation, which are in phase and in antiphase, respectively, with the applied magnetic field. Thus, it is possible to obtain from a SRR array uniform negative response below resonance, by exciting all SRRs in the array to the high-current amplitude state. These remarks are also valid for 2D SRR arrays discussed in the next section.

IV. DISCRETE BREATHERS IN TWO-DIMENSIONAL SRR ARRAYS

Although most of the methodology and techniques for DB construction have been developed for the 1D case, there have been some studies of higher-dimensional systems. Importantly, a rigorous proof of the existence of DBs in higher-dimensional nonlinear lattices was given in Ref. [3]. Numerical studies of DBs have been published for several simple nonlinear lattices, such as, for example, 2D Fermi-Pasta-Ulam chains [50–53], Josephson junction arrays [54], Klein-Gordon chains [55], discrete nonlinear Schrödinger systems [56,57], and also for a Morse lattice [58]. Since most of the present MMs are fabricated in 2D technology, it is necessary to extend the study of magnetoinductive DBs to two dimensions. We see below that neither the Hamiltonian nor the dissipative DBs are destroyed by increasing the dimensionality.

The frequency spectrum of linear MI waves in the 2D system can be obtained as in the 1D case, by substituting a plane wave of the form $q_{n,m}=A\cos(\kappa_x n+\kappa_y m-\Omega\tau)$ into the linearized equations (9) and (10) in the absence of losses and applied field ($\varepsilon_0=0$, $\gamma=0$),

$$\Omega_\kappa = [1 + 2\lambda_x\cos(\kappa_x) + 2\lambda_y\cos(\kappa_y)]^{-1/2}, \qquad (17)$$

where κ_x and κ_y are the (normalized) components of the wave vector in the x and y directions, respectively ($-\pi\leq\kappa_i\leq\pi$, $i=x,y$). In this case, the group velocity is not, in general, in a direction opposite to the phase velocity [34]. Notice that the bandwidth $\Delta\Omega$ depends on both the magnitude of the coupling parameters λ_x and λ_y and their sign. Consider, for example, the case $\lambda_x=\lambda_y=\lambda$ (isotropic lattice in the planar geometry). Then $\Delta\Omega\simeq4|\lambda|$ for $|\lambda|\ll1$, which is larger than that of the corresponding 1D system by a factor of 2. Thus, in this case, the 1D Hamiltonian DBs with frequencies very close to the 1D band may not survive in the 2D case. Typical dispersion curves (i.e., contours of the frequency as a function of κ_x and κ_y) of linear MI waves for isotropic 2D SRR arrays in the planar geometry, anisotropic 2D SRR arrays in the planar geometry, and anisotropic 2D SRR arrays in the planar-axial geometry are shown in the left, middle, and right panels of Fig. 8, respectively. The dispersion equation (17)
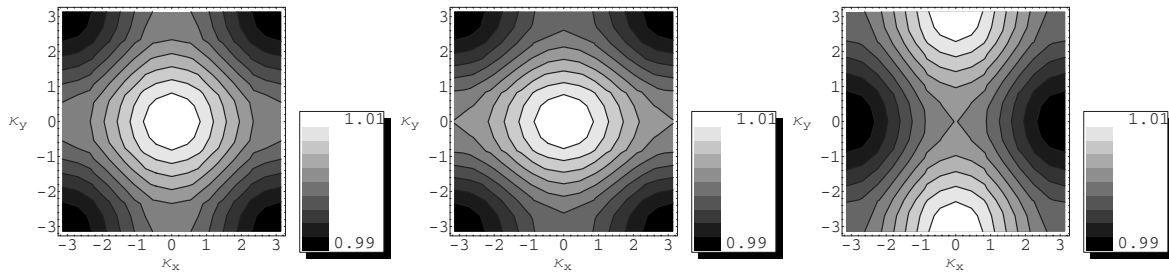
FIG. 8. Dispersion curves of the frequency spectra of linear magnetoinductive waves (along with their corresponding density plots) on the κ_x-κ_y plane [34], for $\lambda_x=\lambda_y=-0.01$ (left panel); $\lambda_x=-0.01, \lambda_y=-0.013$ (middle panel); and $\lambda_x=-0.013, \lambda_y=0.01$ (right panel). In the density plots, darker color indicates lower Ω_κ.
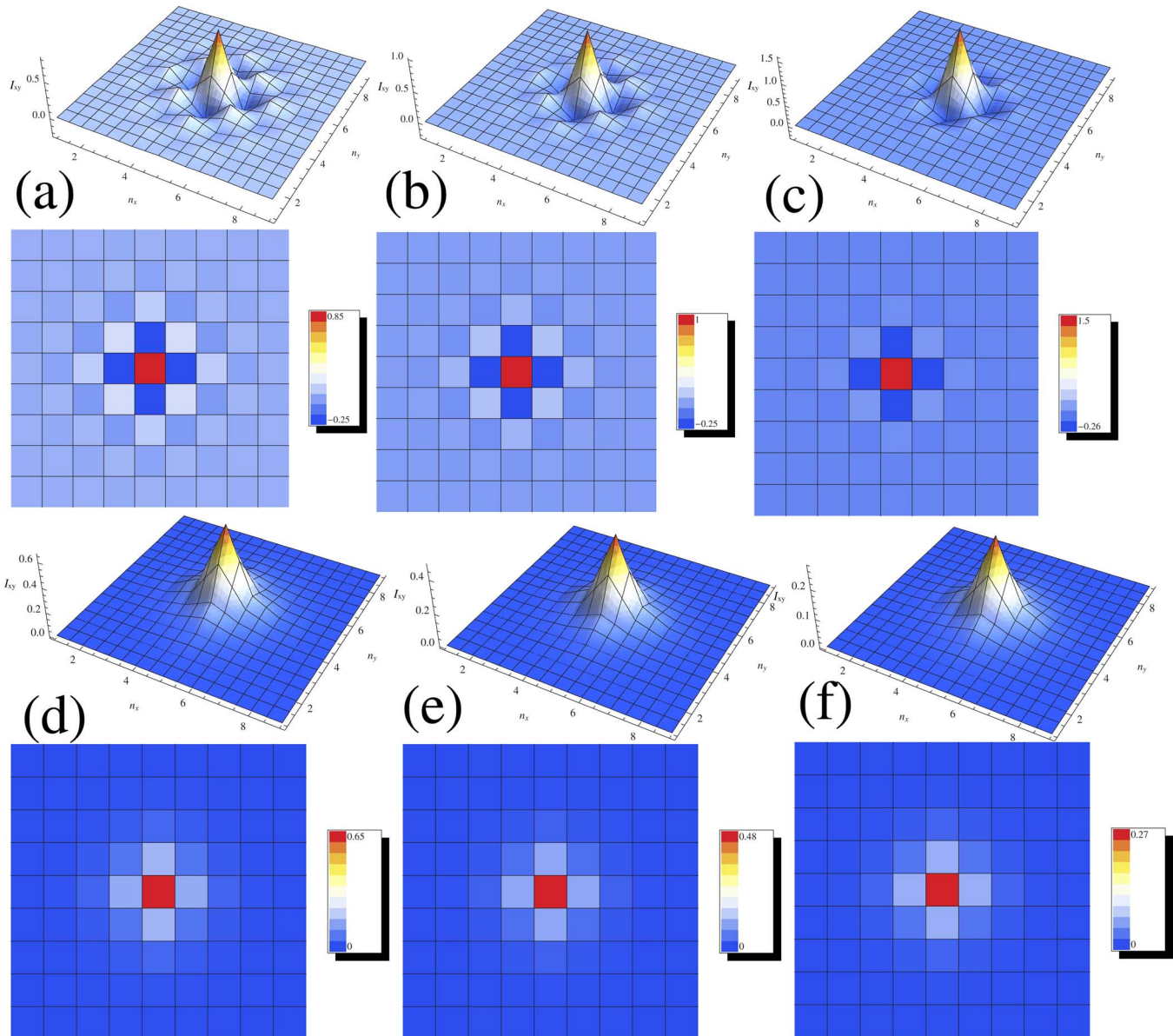

FIG. 9. (Color online) Snapshots of two-dimensional Hamiltonian single-site bright discrete breathers (taken at maximum amplitude), for isotropic split-ring resonator arrays in the planar geometry ($\lambda_x=\lambda_y=\lambda$) with (a) $\alpha=+1$, $\Omega_b=0.952$, $\lambda=-0.020$; (b) $\alpha=+1$, $\Omega_b=0.938$, $\lambda=-0.024$; (c) $\alpha=+1$, $\Omega_b=0.881$, $\lambda=-0.040$; (d) $\alpha=-1$, $\Omega_b=1.082$, $\lambda=-0.025$; (e) $\alpha=-1$, $\Omega_b=1.036$, $\lambda=-0.012$; and (f) $\alpha=-1$, $\Omega_b=1.011$, $\lambda=-0.004$. For each snapshot, the lower panel show the density plot of that discrete breather profile.
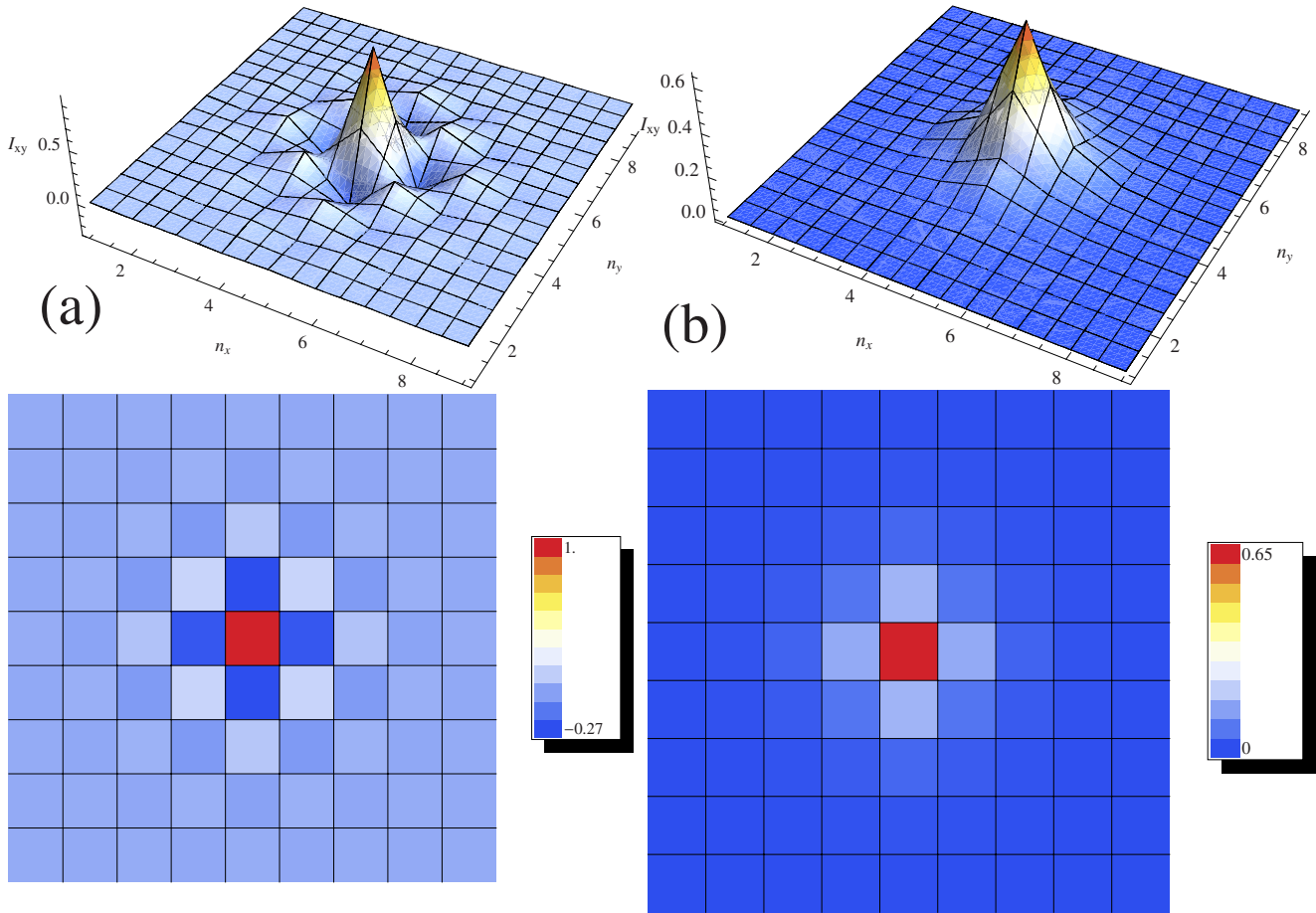
FIG. 10. (Color online) Snapshots of two-dimensional Hamiltonian single-site bright discrete breathers (taken at maximum amplitude), for anisotropic split-ring resonator arrays in the planar geometry with (a) $\alpha = +1$, $\Omega_b = 0.938$, $\lambda_x = -0.024$; $\lambda_y = -0.027$; and (b) $\alpha = -1$, $\Omega_b = 1.082$, $\lambda_x = -0.025$, $\lambda_y = -0.028$. In both (a) and (b), the lower panel show the density plot of the discrete breather profile presented in the corresponding upper panel.

along with the corresponding dispersion curves can also be found in Ref. [34].

For the construction of DBs in 2D arrays, we used the same methods as for the corresponding 1D arrays. We again consider two different geometries of the SRR arrays, the planar geometry [Fig. 2(a)] and the planar-axial geometry [Fig. 2(b)]. In the former geometry, the coupling parameters λ_x, λ_y are both negative. However, they may differ in magnitude, i.e., $|\lambda_x| \neq |\lambda_y|$, as a result of unequal lattice constants d_x and d_y or resulting from the different orientation of the SRRs. In the latter geometry, the coupling parameters have opposite signs, i.e., $\lambda_x < 0$ and $\lambda_y > 0$, which can be regarded as a case of generalized anisotropy. Their magnitudes may, however, be different, depending again on the lattice constants d_x and d_y. In the following we are mainly concerned with single-site bright DBs for both geometries, nonlinearities (self-focusing and self-defocusing), and several DB frequencies and pairs of coupling parameters λ_x, λ_y. However, one may obtain many different types of DBs by just choosing the appropriate initial condition (trivial DB). The 2D array size used in the calculations is typically $N \times N = 15 \times 15$.

Typical Hamiltonian DB profiles in 2D isotropic ($\lambda_x = \lambda_y$) SRR arrays in the planar geometry are shown in the

upper panels of Fig. 9 for both self-focusing [Figs. 9(a)–9(c)] and self-defocusing [Figs. 9(d)–9(f)] nonlinearities. The DB frequencies and coupling parameters are given, for each DB, in the caption of Fig. 9. The lower panels of Figs. 9(a)–9(f) show the density plots of the corresponding DB profiles shown in the upper panels. Notice that, for self-focusing nonlinearity ($\alpha = +1$), the DBs are staggered in both the x and the y directions, while for self-defocusing nonlinearity ($\alpha = -1$), they are unstaggered in both the x and the y directions. We have constructed exact DBs also in the case of an array in the planar geometry with moderate anisotropy, i.e., $\lambda_x \neq \lambda_y$, for both nonlinearities ($\alpha = \pm 1$). Typical DB profiles with the coupling parameters differing by approximately 10% are shown in Figs. 10(a) and 10(b) (upper panels) for $\alpha = +1$ and -1, respectively. The anisotropy does not change the staggered or unstaggered character of these DBs, which remain staggered (unstaggered) in both directions for $\alpha = +1$ (-1). The lower panels of Figs. 10(a) and 10(b) show the density plots of the corresponding DB profiles shown in the upper panels. In those density plots, a DB that is staggered in both directions appears as a checkerboard rotated by 45° with respect to the array.
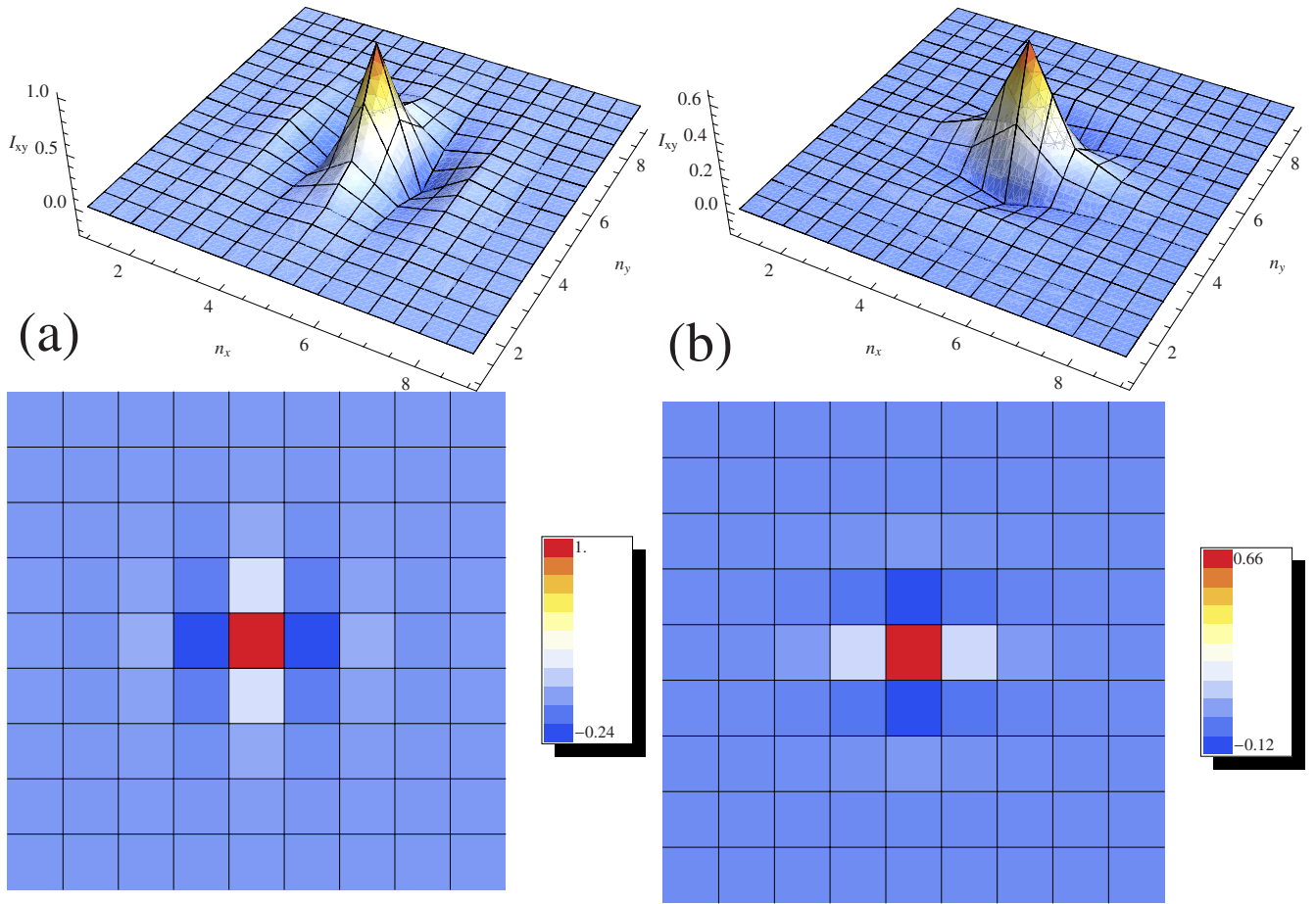
FIG. 11. (Color online) Snapshots of two-dimensional Hamiltonian single-site bright discrete breathers (taken at maximum amplitude), for anisotropic split-ring resonator arrays in the planar-axial geometry with (a) $\alpha=+1$, $\Omega_b=0.938$, $\lambda_x=-0.024$; $\lambda_y=0.021$; and (b) $\alpha=-1$, $\Omega_b=1.082$, $\lambda_x=-0.025$, $\lambda_y=0.022$. In both (a) and (b), the lower panel show the density plot of the discrete breather profile presented in the corresponding upper panel.

Typical Hamiltonian DB profiles in 2D anisotropic ($|\lambda_x| \neq |\lambda_y|$) SRR arrays in the planar-axial geometry are shown in the upper panels of Figs. 11(a) and 11(b) for $\alpha=+1$ and -1, respectively, along with their corresponding density plots (lower panels). The coupling parameters differ in magnitude by approximately 10%. In this case we observe that for $\alpha=+1$ (-1) the DB is staggered (unstaggered) along the x (y) direction, while it is unstaggered (staggered) along the y (x) direction. Thus, the change in either the sign of the nonlinearity α or the sign of the coupling parameter λ_y leads to a change in the staggered or unstaggered character of a DB in the y direction. Specifically, by changing α from $+1$ to -1 (for $\lambda_y>0$), a DB unstaggered in the y direction becomes staggered in that direction, while by changing α from -1 to $+1$ (for $\lambda_y>0$), a DB staggered in the y direction becomes unstaggered in that direction. Also, by changing λ_y from positive to negative (for $\alpha=+1$), a DB unstaggered in the y direction becomes staggered in that direction, while by changing λ_y from negative to positive (for $\alpha=+1$), a DB staggered in the y direction becomes unstaggered in that direction. The linear stability of all the Hamiltonian DBs presented in this section is checked through Floquet analysis (finding the eigenvalues of the Floquet matrix), and they were found to be linearly stable.

Typical examples of dissipative DB profiles in 2D isotropic ($\lambda_x=\lambda_y$) SRR arrays in the planar geometry, 2D anisotropic ($\lambda_x \neq \lambda_y$) SRR arrays in the planar geometry, and 2D anisotropic ($|\lambda_x| \neq |\lambda_y|$) SRR arrays in the planar-axial geometry are shown in Figs. 12(a)–12(c), respectively, for $\alpha=+1$. These profiles are actually snapshots at some specific instant during the DB motion. Here, just as in the 1D case, both the background and the DB (i.e., the central DB site) oscillate with low and high current amplitudes, respectively, at the same frequency $\Omega_b=\Omega$. The lower panels of Figs. 12(a)–12(c) show the density plots of the corresponding DB profiles shown in the upper panels. The stability of the dissipative DBs has been checked by adding small perturbations of the order of 10^{-2} and following their time evolution for long time intervals (over $10^3 T_b$ time units). In all cases it was found that the DBs are not destroyed by the perturbation but, instead, they return to their unperturbed shape.

The magnetic response of the dissipative 2D arrays can be calculated as in the 1D case, with the help of Eq. (16) applied locally at each array cell (n,m). In Fig. 13 we plot separately the time evolution of each of the three terms of Eq. (16), i.e., the instantaneous magnetic induction, the applied magnetic field, and the magnetic response, at the central DB site [Figs. 13(b), 13(d), and 13(f) high-amplitude
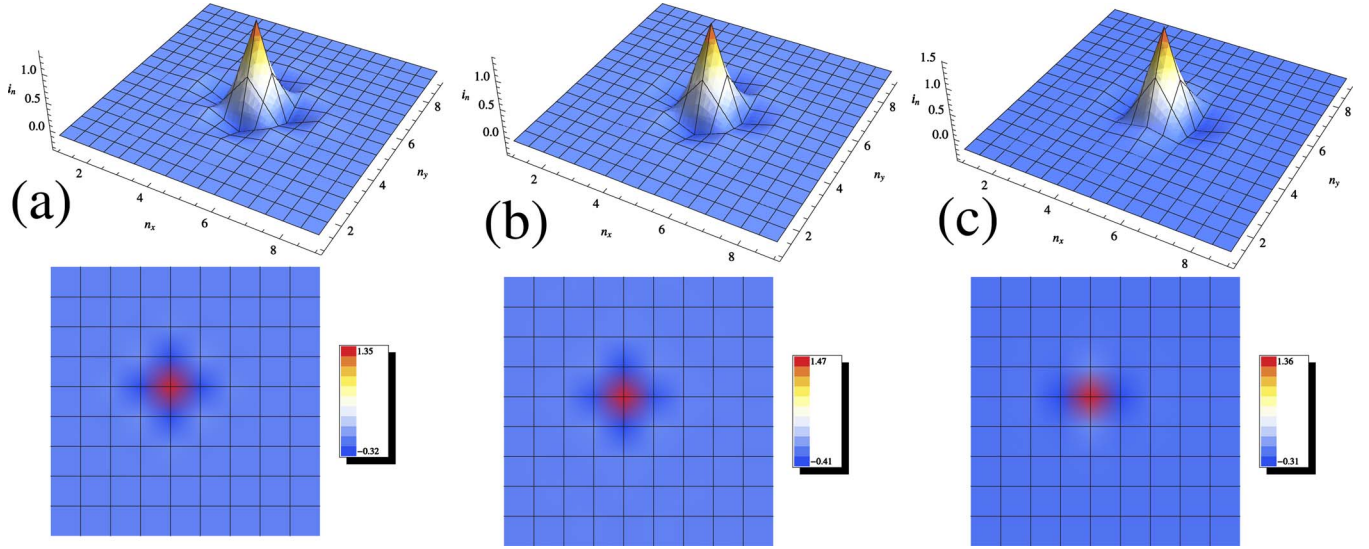
FIG. 12. (Color online) Snapshots of two-dimensional dissipative (single-site, bright) discrete breathers (taken at maximum amplitude), for $\alpha = +1$, $\Omega_b = 0.92$, $\varepsilon_0 = 0.04$, $\gamma = 0.01$, $\epsilon_\ell = 2$ and (a) $\lambda_x = \lambda_y = -0.02$ (isotropic split-ring resonator arrays in the planar geometry); (b) $\lambda_x = -0.02, \lambda_y = -0.023$ (anisotropic split-ring resonator arrays in the planar geometry); (c) $\lambda_x = -0.0124, \lambda_y = 0.0094$ (anisotropic split-ring resonator arrays in the planar-axial geometry). For each snapshot, the lower panel shows the density plot of the discrete breather profile presented in the corresponding upper panel.

current oscillation] and at the site with $n, m = 3, 5$ [Figs. 13(a), 13(c), and 13(e) low-amplitude current oscillation] for the three DBs shown in Fig. 12. The results look the same for the first two cases, corresponding to isotropic 2D SRR arrays
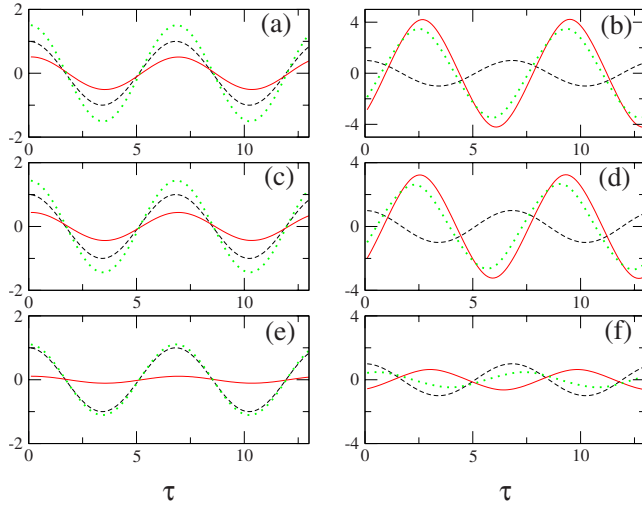

FIG. 13. (Color online) Time evolution of $\ell i_n(\tau)$ (red solid curve), compared with $\cos(\Omega \tau)$ (black dashed curve), and their sum (green dotted curve), during two breather periods, for a 2D SRR array (a) in the planar configuration at $(n,m) = (3,5)$ ($\lambda_x = \lambda_y = -0.02$, $\ell = 3$); (b) in the planar configuration at the central breather site ($\lambda_x = \lambda_y = -0.02$, $\ell = 3$); (c) in the planar configuration at $(n,m) = (3,5)$ ($\lambda_x = -0.02$, $\lambda_y = -0.023$, $\ell = 2.6$); (d) in the planar configuration at the central breather site ($\lambda_x = -0.02$, $\lambda_y = -0.023$, $\ell = 2.6$); (e) in the planar-axial configuration at $(n,m) = (3,5)$ ($\lambda_x = -0.0124$, $\lambda_y = 0.0094$, $\ell = 0.43$); (f) in the planar-axial configuration at the central breather site ($\lambda_x = -0.0124$, $\lambda_y = 0.0094$, $\ell = 0.43$). The other parameters are as in Fig. 12.

in the planar geometry [Figs. 13(a) and 13(b)], and anisotropic 2D SRR arrays in the planar geometry [Figs. 13(c) and 13(d)]. They are also similar to those calculated for the corresponding 1D case. The SRRs with low-amplitude current oscillation $[(n,m) = (3,5)]$ show a positive (paramagnetic) response while the SRR with high-amplitude current oscillation (central DB site) shows an extreme diamagnetic (negative) response. In the third case, however, for anisotropic 2D SRR arrays in the planar-axial geometry [Figs. 13(e) and 13(f)], the response of the SRR with high-amplitude current oscillation is still diamagnetic but not negative. This is due to the very weak coupling which presumes relatively large separation of the SRRs, and thus a very low-density SRR array. Guided by the previous results, we consider the possibility of constructing a region in a 2D SRR array with extreme diamagnetic (negative) response, surrounded by a paramagnetic background. For this purpose we may exploit a bright 2D multibreather consisting of a number of adjacent sites (SRRs) in the center of the array. For illustration, such a multibreather occupying a region of nine sites (including the central one) in an isotropic SRR array in the planar geometry, is shown in Fig. 14. We have checked that, indeed, the sites with high-amplitude current oscillation show negative magnetic response, while the rest of them show positive magnetic response. The lower panel shows the density plot of the multibreather profile shown in the upper panel. Thus, it seems possible to create SRR-based MMs with distinct regions of opposite-sign magnetic responses by exploiting multibreathers.

The numerical results for both 1D and 2D SRR arrays reveal that, at least for weak coupling, the amplitude and the time dependence of the central DB site and the background are essentially those of the single damped driven SRR oscillator. Only the first one or two sites neighboring the central DB site exhibit significant differences due to the coupling.
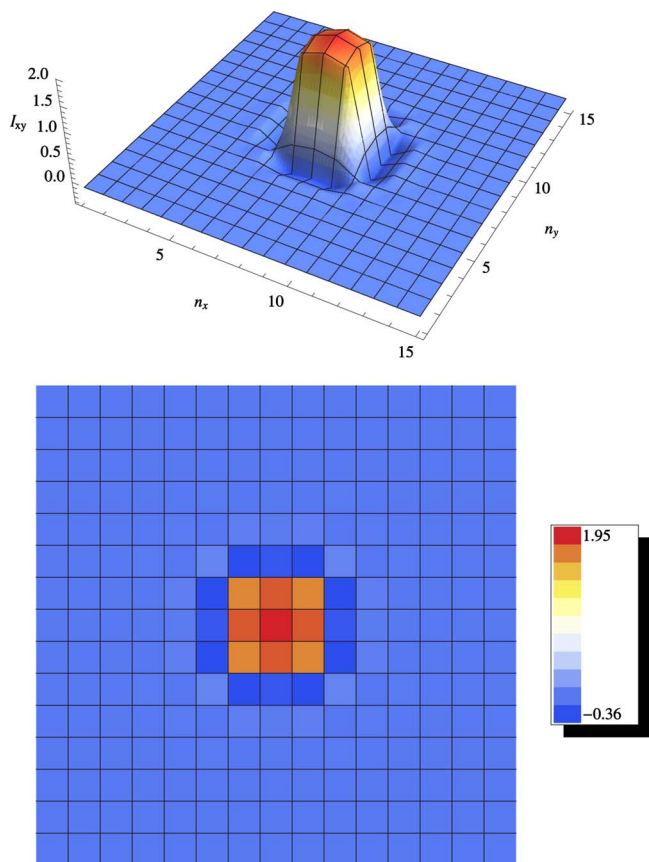
FIG. 14. (Color online) Upper panel: A snapshot of a two-dimensional dissipative multibreather (taken at maximum amplitude), constructed for a split-ring resonator array in the planar geometry, for $\lambda_x = \lambda_y = -0.02$, $\omega_b = 0.92$, $\varepsilon_0 = 0.04$, $\gamma = 0.01$, $\epsilon_\ell = 2$, $\alpha = +1$. Lower panel: density plot of the multibreather profile shown in the upper panel.

The bistability of the single SRR oscillator, which is important for the construction of dissipative DBs and also for the creation of uniform states with either positive or negative magnetic response below resonance, is not restricted to frequencies close to resonance. In Fig. 15 we show the time evolution of i_n of two coexisting and stable states far from resonance, along with the normalized driving magnetic field. Dissipative DBs can be constructed by combining these two
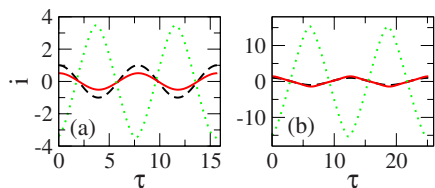

FIG. 15. (Color online) Time evolution of the normalized driving term $\cos(\Omega \tau)$ (black dashed curve), and the current $i(\tau)$ for the low- and high-current amplitude states (red solid and green dotted curves, respectively) for a single damped driven SRR oscillator with $\gamma = 0.01$, $\epsilon_\ell = 2$, $\alpha = +1$ and (a) $\Omega = 0.8$, $\varepsilon_0 = 0.2$; (b) $\Omega = 0.5$, $\varepsilon_0 = 1.2$.

states into a trivial DB and continuing that solution for finite (nonzero) coupling parameters. Although for the cases shown the current of the high-amplitude current state is rather large, where the saturation of the nonlinear term could be expected, Fig. 15 indicates that it is possible to obtain negative response below resonance by exciting the SRRs in that state.

V. CONCLUSIONS

We considered a simple model for nonlinear SRR-based MMs in one and two dimensions, where the nonlinearity arises from a Kerr-type dielectric which fills the SRR slits. Each SRR is modeled as a nonlinear *RLC* electrical circuit driven by an alternating voltage source, weakly coupled to its nearest neighbors due to magnetic interactions through their mutual inductance *M* (magnetoinductive coupling). The sign of the coupling between neighboring SRRs depends on their relative orientation within the SRR array.

We have constructed, using standard numerical methods, many different types of Hamiltonian and dissipative DBs in both 1D and 2D arrays for different nonlinearities (i.e., self-focusing and self-defocusing), and different geometries (planar-axial in 1D, planar and planar-axial in 2D). We have also constructed DBs in 2D arrays with moderate anisotropy. Most of the DBs presented here are linearly stable under small perturbations. Dissipative SRR arrays, driven by an applied magnetic field, offer the possibility of studying their magnetic response with respect to that field. The induced current oscillations are proportional to the magnetic moments of the SRRs and, thus, to the local magnetization (magnetic response) of the array. We found that low-(high-)amplitude current oscillations are in phase (almost in antiphase) with the applied field. Thus, depending on the array and the external field parameters, the magnetic response at the SRRs with high-amplitude current oscillation can be negative. In this way, DBs can change the magnetic response of the array locally from paramagnetic to extremely diamagnetic. By exploiting multibreathers, it seems possible to create SRR-based MMs with distinct regions of opposite-sign magnetic responses.

The bistability due to nonlinearity is not restricted to frequencies close to resonance, but is found to persist down to much lower frequencies. As a result, dissipative DBs with frequencies and external field amplitudes in rather wide intervals can be constructed. Moreover, even far from resonance, the coexisting and stable low- and high-current amplitude states are in phase and in antiphase, respectively, with the applied magnetic field. Thus, it seems possible to get uniform solutions at these low frequencies, which provide either positive or negative magnetic response below resonance. This could be achieved by exciting all the SRRs in the low- or high-amplitude state, respectively.

[1] S. Flach and C. R. Willis, Phys. Rep. **295**, 181 (1998).

[2] A. J. Sievers and S. Takeno, Phys. Rev. Lett. **61**, 970 (1988).

[3] R. S. MacKay and S. Aubry, Nonlinearity **7**, 1623 (1994).

[4] S. Aubry, Physica D **103**, 201 (1997).

[5] J. L. Marín and S. Aubry, Nonlinearity **9**, 1501 (1996).

[6] J. L. Marín, F. Falo, P. J. Martínez, and L. M. Floría, Phys. Rev. E **63**, 066603 (2001).

[7] D. Zueco, P. J. Martínez, L. M. Floría, and F. Falo, Phys. Rev. E **71**, 036613 (2005).

[8] M. Peyrard, Physica D **119**, 184 (1998).

[9] G. P. Tsironis and S. Aubry, Phys. Rev. Lett. **77**, 5225 (1996).

[10] K. Ø. Rasmussen, S. Aubry, A. R. Bishop, and G. P. Tsironis, Eur. Phys. J. B **15**, 169 (2000).

[11] K. Ø. Rasmussen, D. Cai, A. R. Bishop, and N. Grønbech-Jensen, Europhys. Lett. **47**, 421 (1999).

[12] D. Hennig, L. Schimansky-Geier, and P. Hänggi, Europhys. Lett. **78**, 20002 (2007).

[13] B. I. Swanson, J. A. Brozik, S. P. Love, G. F. Strouse, A. P. Shreve, A. R. Bishop, W.-Z. Wang, and M. I. Salkola, Phys. Rev. Lett. **82**, 3288 (1999).

[14] U. T. Schwarz, L. Q. English, and A. J. Sievers, Phys. Rev. Lett. **83**, 223 (1999).

[15] E. Trías, J. J. Mazo, and T. P. Orlando, Phys. Rev. Lett. **84**, 741 (2000).

[16] M. Sato, B. E. Hubbard, A. J. Sievers, B. Ilic, D. A. Czaplewski, and H. G. Craighead, Phys. Rev. Lett. **90**, 044102 (2003).

[17] H. S. Eisenberg, Y. Silberberg, R. Morandotti, A. R. Boyd, and J. S. Aitchison, Phys. Rev. Lett. **81**, 3383 (1998).

[18] J. Edler, R. Pfister, V. Pouthier, C. Falvo, and P. Hamm, Phys. Rev. Lett. **93**, 106405 (2004).

[19] G. P. Tsironis, Chaos **13**, 657 (2003).

[20] G. Kopidakis, S. Aubry, and G. P. Tsironis, Phys. Rev. Lett. **87**, 165501 (2001).

[21] S. Flach and K. Kladko, Physica D **127**, 61 (1999).

[22] D. Chen, S. Aubry, and G. P. Tsironis, Phys. Rev. Lett. **77**, 4776 (1996).

[23] F. M. Russell and J. C. Eilbeck, Europhys. Lett. **78**, 10004 (2007).

[24] M. Sato and A. J. Sievers, Phys. Rev. Lett. **98**, 214101 (2007).

[25] P. J. Martínez, M. Meister, L. M. Floria, and F. Falo, Chaos **13**, 610 (2003).

[26] P. J. Martínez, L. M. Floría, F. Falo, and J. J. Mazo, Europhys. Lett. **45**, 444 (1999).

[27] N. Lazarides, M. Eleftheriou, and G. P. Tsironis, Phys. Rev. Lett. **97**, 157406 (2006).

[28] T. J. Yen, W. J. Padilla, N. Fang, D. C. Vier, D. R. Smith, J. B. Pendry, D. N. Basov, and X. Zhang, Science **303**, 1494 (2004).

[29] V. A. Podolskiy, A. K. Sarychev, and V. M. Shalaev, Opt. Express **11**, 735 (2003).

[30] C. M. Soukoulis, S. Linden, and M. Wegener, Science **315**, 47 (2007).

[31] E. Shamonina, V. A. Kalinin, K. H. Ringhofer, and L. Solymar, J. Appl. Phys. **92**, 6252 (2002).

[32] M. J. Freire, R. Marqués, F. Medina, M. A. G. Laso, and F. Martín, Appl. Phys. Lett. **85**, 4439 (2004).

[33] O. Sydoruk, O. Zhuromskyy, E. Shamonina, and L. Solymar, Appl. Phys. Lett. **87**, 072501 (2005).

[34] R. R. A. Syms, E. Shamonina, and L. Solymar, Eur. Phys. J. B **46**, 301 (2005).

[35] A. A. Zharov, I. V. Shadrivov, and Y. S. Kivshar, Phys. Rev. Lett. **91**, 037401 (2003).

[36] S. O'Brien, D. McPeake, S. A. Ramakrishna, and J. B. Pendry, Phys. Rev. B **69**, 241101(R) (2004).

[37] M. Lapine, M. Gorkunov, and K. H. Ringhofer, Phys. Rev. E **67**, 065601(R) (2003).

[38] I. V. Shadrivov, S. K. Morrison, and Y. S. Kivshar, Opt. Express **14**, 9344 (2006).

[39] I. V. Shadrivov, A. N. Reznik, and Y. S. Kivshar, Physica B **394**, 180 (2007).

[40] I. V. Shadrivov, A. A. Zharov, N. A. Zharova, and Y. S. Kivshar, Photonics Nanostruct. Fundam. Appl. **4**, 69 (2006).

[41] I. Kourakis, N. Lazarides, and G. P. Tsironis, Phys. Rev. E **75**, 067601 (2007).

[42] N. Lazarides and G. P. Tsironis, Appl. Phys. Lett. **90**, 163501 (2007).

[43] N. Katsarakis, G. Konstantinidis, A. Kostopoulos, R. S. Penciu, T. F. Gundogdu, M. Kafesaki, E. N. Economou, Th. Koschny, and C. M. Soukoulis, Opt. Lett. **30**, 1348 (2005).

[44] O. Sydoruk, A. Radkovskaya, O. Zhuromskyy, E. Shamonina, M. Shamonin, C. J. Stevens, G. Faulkner, D. J. Edwards, and L. Solymar, Phys. Rev. B **73**, 224406 (2006).

[45] R. R. A. Syms, O. Sydoruk, E. Shamonina, and L. Solymar, Metamaterials **1**, 44 (2007).

[46] F. Hesmer, E. Tatartschuk, O. Zhuromskyy, A. A. Radkovskaya, M. Shamonin, T. Hao, C. J. Stevens, G. Faulkner, D. J. Edwards, and E. Shamonina, Phys. Status Solidi B **244**, 1170 (2007).

[47] N. Lazarides, G. P. Tsironis, and M. Eleftheriou, e-print arXiv:0712.0719v1.

[48] A. Alvarez, J. F. R. Archilla, J. Cuevas, and F. R. Romero, New J. Phys. **4**, 72 (2002).

[49] A. Maluckov, M. Stepić, D. Kip, and Lj. Hadzievski, Eur. Phys. J. B **45**, 539 (2005).

[50] S. Flach, K. Kladko, and S. Takeno, Phys. Rev. Lett. **79**, 4838 (1997).

[51] J. L. Marín, J. C. Eilbeck, and F. M. Russel, Phys. Lett. A **248**, 225 (1998).

[52] R. Sarkar and B. Dey, J. Phys. A **39**, L99 (2006).

[53] I. A. Butt and J. A. D. Wattis, J. Phys. A **40**, 1239 (2007).

[54] J. J. Mazo, Phys. Rev. Lett. **89**, 234101 (2002).

[55] V. M. Burlakov, S. A. Kiselev, and V. N. Pyrkov, Phys. Rev. B **42**, 4921 (1990).

[56] P. G. Kevrekidis, K. Ø. Rasmussen, and A. R. Bishop, Phys. Rev. E **61**, 2006 (2000).

[57] J. Gómez-Gardeñes, L. M. Floría, and A. R. Bishop, Physica D **216**, 31 (2006).

[58] K. Ikeda, Y. Doi, B.-F. Feng, and T. Kawahara, Physica D **225**, 184 (2007).